

## Zinc oxide thin films preparation by chemical methods onto Si substrate for solar cell application

A. I. Aljameel\*, M. K. M. Ali

*Department of Physics, College of Science, Imam Mohammad Ibn Saud Islamic University (IMSIU), P.O. Box 90950, Riyadh 11623, Saudi Arabia*

In this work, solar cell devices have been fabricated based on three n-type zinc oxide (ZnO) thin films deposited on p-type Si (111) substrate. ZnO thin films were spin-coated on ZnO seed layer coated Si(111) substrates using chemical solutions that consist of ZnO nanoparticles. ZnO nanoparticle solutions were prepared via three various chemical methods, which are co-precipitation, the sol-gel and the combustion method. The coated films were gradually calcinated to liftoff the solvent then annealed at 700 °C for 3 hours. The produced samples' structural properties and surface morphology were investigated using field-emission scanning electron microscopy (FESEM) and X-ray diffractometry (XRD). Simultaneously, the optical and electrical characteristics were studied using UV-Visible spectrometer and Hall effect measurement, respectively. The performance of these three kinds of solar cells was computed.

(Received March 21, 2021; Accepted June 15, 2021)

*Keywords: ZnO; p-type Si; solar cell; thin films*

### 1. Introduction

The chemical preparation methods such chemical bath, precipitation, sol-gel conditions, and combustion method are wide used and powerful technique to synthesis ZnO NPs [1-4]. These processes are mainly used in aqueous medium consist salts of zinc acetate or zinc nitrate or and hexamine under heating at temperature below 100°C [5, 6]. The variation of the concentration, the pH, of growth solution thermal treatment growth rate are consider variables to modified or change the resulting ZnO nanostructures. For homogeneous growth of ZnO crystals, deposition of very low dimension of ZnO thin film as a seed layer on substrates creates the starting point of the synthesis and nucleation.

In the present work, we have developed ZnO thin film from an aqueous solution of a zinc complex. the films are spin coted onto Si substrates to fabricate thee solar cell device and studied the effect of corresponding structural, optical and electrical properties ZnO NP on the solar cell performance. This report may give an added impetus on the applications of this technologically important material and give newer alternatives to optoelectronics industries.

### 2. Experimental section

#### 2.1 Materials

All chemical reagents employed in this work were analytical grade, acquired from Sinopharm Chemical Reagent Corp, P. R. China, and were utilized without additional purification. Water purified by a Milli-Q water system (Millipore) was applied everywhere.

#### 2.2. Fabrication details

##### 2.2.1. ZnO p nanoparticles thin film obtained from precipitation method

Zinc oxide (ZnO) nanoparticles was fabricated using a co-precipitation method through zinc acetate dehydrate as starting materials. A 39.9 mmole of zinc acetate dihydrate aqueous

---

\* Corresponding author: abo\_anas\_1@yahoo.com

solution was dissolved in a 100 ml deionized water beneath magnetically stirring settings. Afterward 40 min, 12 mmole of NaOH solution was added drop-wise to the zinc acetate aqueous solution and the last solutions were shaking for extra 15 min. Lastly, the formed precipitate was washed thrice with water ethanol combination (1:1) and the white precipitate was spin coated onto p-type Si (111), drained at 105°C for 10 h and annealed under Oxygen flowing at 500°C for 3h.

### **2.2.2. ZnO s nanoparticles thin film obtained from sol-gel method**

For the preparation of ZnO via the sol-gel method [7], 39.9 mmole of zinc acetate was dissolved in (3:1) methanol-water solution and stirred for 15 min till all solids became dissolved. Later that, 30 ml of saturated starch solution was added dropwise to the opening materials underneath vigorous magnetic stirring for 30 min until sol made. Meanwhile, 60 ml of 66 mmoles of the aqueous tartaric acid solution were supplemented dropwise until the gel was produced. The collected gel was spin coated onto p-type Si (111) then kept at room temperature for 2h and drained at 105°C for 10h. Afterward, the produced thin films annealed at 500°C for 3h.

### **2.2.3. ZnO c nanoparticles obtained from combustion method**

Through the simple fabrication process of ZnO nanoparticles using the combustion method, 39.9 mmole of zinc acetate dihydrate solution was stirred well for 30 min. 33.3 mmole of arabinose solution was then added dropwise to the starting materials under vigorous shaking at 90°C for 6h until small a brown-white particle start to formed. The produced mixer was cooled at room temperature and then spin coated for thee runs onto p-type Si (111). Following a few minutes drained at 105°C for 2h. The received films annealed at 500°C 3h to get zinc oxide nanomaterials thin films.

## **2.3. Characterization of ZnO p, ZnO s, and ZnO c nanoparticles**

The phase structural and crystallite sizes of ZnO nanomaterials were investigated using X-ray diffraction (XRD, Perkin Elmer) through CuK $\alpha$  radiation. The surface characteristics of all samples were recorded via Brunauer-Emmett-Teller (BET) method. The morphology and elemental compositions of samples was examined applied Field Scanning Electron Microscopy (FE-SEM, JEOL-6700F) and energy dispersive X-ray spectrometer (EDX). The UV-visible absorption and diffuse reflectance spectra (DRS) were estimated using the JASECO V-770 spectrophotometer in the wavelength range 200-800 nm. The chemical vibration and bending of the fabricated samples were determined employed Fourier transform infrared spectroscopy (Model: Nicolet 6700) in the range 4000 - 400 cm<sup>-1</sup> with a resolution of 4 cm<sup>-1</sup>.

## **3. Results and discussion**

### **3.1. XRD analysis**

Fig. 1 depicts the X-ray diffraction patterns of the ZnO samples fabricated using different approaches. The findings prove the formation of the ZnO nanoparticles after calcination at the fixed annealing temperature. It points that the XRD patterns of all specimens have hexagonal wurtzite formation which verified through JCPDS card no: 01-076-0704 [8]. Further peaks are not existing for all samples, which designated that the ultimate outcomes are purely ZnO phase [9]. Fig. 1 also reveals that all diffraction peaks are relatively strong and indicating an excellent crystallinity for all specimens. The average crystallite size of all ZnO samples corresponding to principal peak at (101) are computed utilizing the Debye-Scherer equation:

$$D = \frac{0.9\lambda}{\beta \cos\theta} \quad (1)$$

where D(nm) is indicated crystallite size, K is designated Scherer constant depends on the shape factor which it is considered equal to 0.9, and  $\lambda$  is symbolizes wavelength of the X-ray employing Cu K $\alpha$  radiation (0.15406 nm), and theta ( $\theta$ ) is represented Bragg's diffraction angle in degree and  $\beta$  is meant Full-Width Half-Maximum (FWHM) in radian of the corresponding peak [10]. The

medium crystallite size was assessed as 19.56 nm, 26.32 nm, and 18.23 nm for ZnO p, ZnO s, and ZnO c, individually.

The d- spacing magnitude was computed from the famous Bragg's formula:

$$d = \frac{\lambda}{2 \sin \theta} \quad (2)$$

And the lattice parameters (a) and (b) were collected through the following's equations [11]:

$$a = \frac{\lambda}{\sqrt{3} \sin \theta} \text{ and } c = \frac{\lambda}{\sin \theta} \quad (3)$$

and the volume of unit cell was determined via equation:

$$V = 0.866 \times a^2 \times c \quad (4)$$

Strain and stress  $\sigma$  (GPa) in the crystallite's plane estimated from equations (5) and (6) [12]:

$$\varepsilon = \frac{\beta}{4 \tan \theta} \quad (5)$$

$$\sigma = 233 \left( \frac{c_{bulk} - c}{c_{bulk}} \right) \quad (6)$$

Zn – O bond length of samples calculated using following formula [13]

$$L = \sqrt{\left[ \frac{a^3}{3} + (0.5 - u)^2 * c^2 \right]} \quad (7)$$

where

$$u = \frac{a^2}{3c^2} + 0.25$$

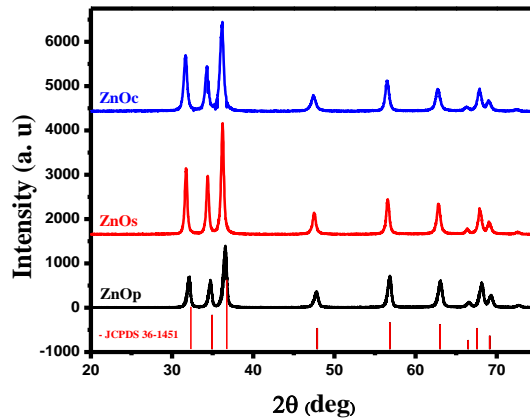


Fig 1. (a) XRD patterns of the all samples.

Table 1. The variation of XRD parameters of nanomaterials.

Samples	ZnO p	ZnO s	ZnO c
<b>2θ (101)</b>	36.55	36.21	36.13
<b>β</b>	0.447	0.3304	0.479
<b>D (nm)</b>	19.56	26.32	18.23
<b>Lattice (a)</b>	3.2211	3.2541	3.2572
<b>Lattice (c)</b>	5.1648	5.2124	5.2221
<b>a/c</b>	1.6034	1.6018	1.6033
<b>d- spacing</b>	2.4564	2.4488	2.484
<b>v</b>	46.41	47.47	47.97
<b>u</b>	0.3788	0.3799	0.3778
<b>L</b>	1.9622	1.9803	1.9742

### 3.2. Morphology (SEM) and elemental (EDX) investigations

The morphology of the fabricated ZnO thin films employed different methods are depicted via SEM in Fig. 2(a-c). The ZnO nanoparticles' SEM micrographs obtained from the precipitation method displayed elongated nanoflakes of rod-shaped features and distribution nanoparticles homogeneities. Whereas the ZnO nanomaterials received using the sol-gel method illustrated semi-spherical shape. The ZnO nanoparticles prepared via the combustion method showed spherical shape at room temperature. To investigate the composition and cleanliness of ZnO prepared by all methods, the EDX analysis was applied. The spectrum of three ZnO samples calcined at 700°C (Fig. 2(d-f)) apparently confirmed a strong acknowledgment at 1 and 0.5 KeV associated with Zn and O, sequentially. Besides, a small band at 8.6 and 9.5 were also due to Zn.

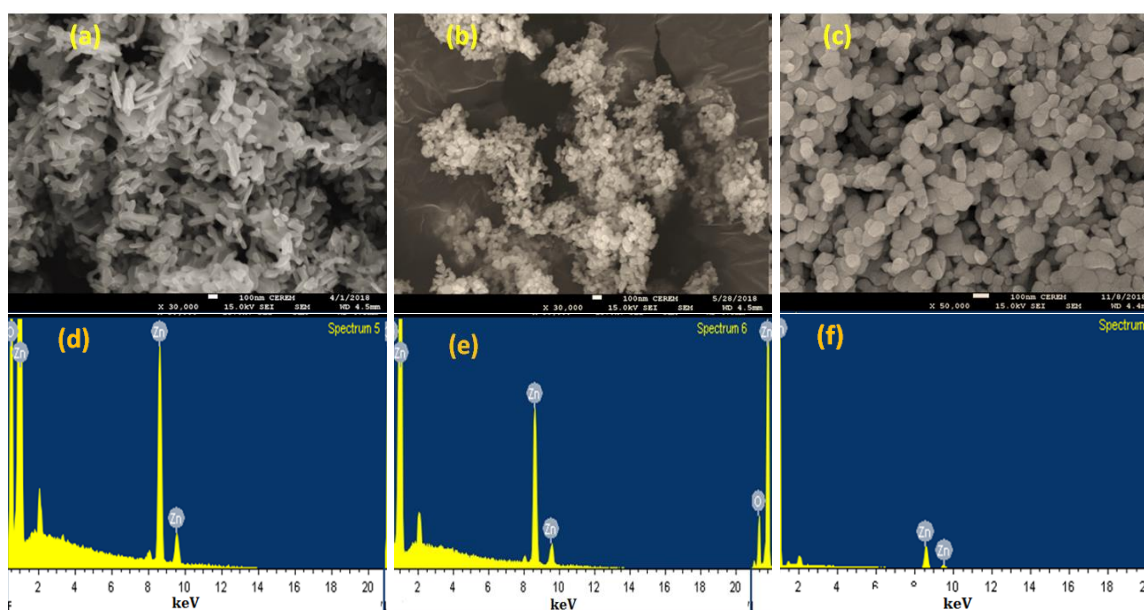


Fig. 2. (a-c) SEM images and (d- f) elemental mapping (EDX) of all ZnO samples.

### 3.3. BET surface area analysis

Fig. 3a manifests the N<sub>2</sub> adsorption-desorption isotherms and pore size distribution of all ZnO specimens. As viewed, both isotherms are identified as type IV beside the hysteresis loop. The BET surface area of ZnO p, ZnO s, and ZnO c nanoparticles was 10.7, 7.6, and 12.3 m<sup>2</sup>/g, respectively, which depends on the preparation method. The high specific surface area is observed for ZnO fabricated through the precipitation, sol-gel, and combustion procedure.

The BJH model has been computed for the assessment of the pore size distribution for the fabricated nanoparticles. As portrayed in Fig. 3b and Table 2. All specimens pore size and pore volumes were computed as 0.055, 0.067, and 0.053 ( $\text{cm}^3/\text{g}$ ), sequentially. The pore size distribution of ZnO p, ZnO s, and ZnO c nanoparticles is well-dispersed in the interval 20 to 50 nm.

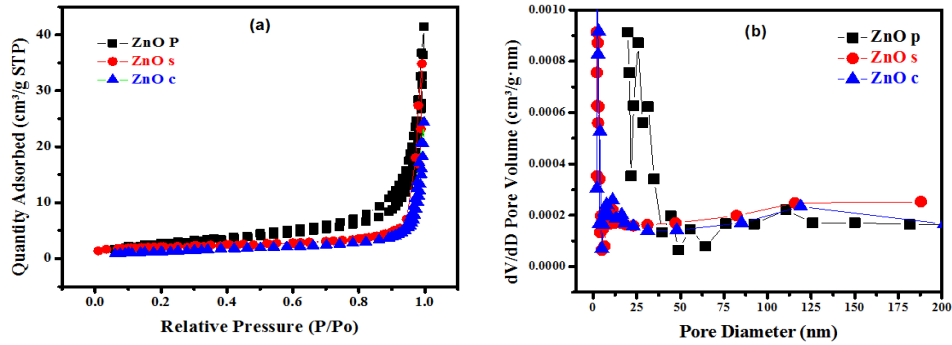


Fig. 3. (a) Adsorption-desorption isotherms of  $\text{N}_2$  at 77 K, and (b) pore size distribution.

Table 2. BET surface area characteristics of the nanoparticles.

Samples	BET Surface area ( $\text{m}^2/\text{g}$ )	Pore volume ( $\text{cm}^3/\text{g}$ )	Average pore diameter(nm) Adsorption - Desorption
ZnO p	10.7	0.055	43.03 - 39.38
ZnO s	7.6	0.067	27.63 - 34.67
ZnO c	12.3	0.053	36.03 - 32.58

### 3.4. Optical analysis

#### 3.4.1. UV-visible and DRS determination

The UV-visible absorption spectra for all specimens are manifested in Fig. 4a. The obtained results of the absorption peaks positioned at 381 nm, 369 nm and 376 nm for ZnO p, ZnO s, and ZnO c, respectively. The Energy band-gap ( $E_g$ ) for all ZnO samples prepared using different methods can be achieved through plotting the correlation between  $(\alpha h\nu)^2$  and  $h\nu$ , which described as the Tauc's law formula [14].

$$(\alpha h\nu)^{1/n} = A(h\nu - E_g) \quad (8)$$

where  $h$  is the Planck's constant,  $\nu$  is represented the frequency,  $\alpha$  is symbolized the absorption coefficient,  $E_g$  is the band gap energy in eV,  $A$  is proportionality consistent, and  $n$  relates to the type of electron transition (for directly enabled transitions,  $n = 1/2$ ). As portrayed in Fig. 4b, the magnitude energy band gap was determined to be 3.21, 3.18, and 3.23 eV for ZnO p, ZnO s, and ZnO c, respectively. It can be remarked that the value of ZnO s prepared using the sol-gel method showed a lower value of 3.18 compared with other samples. This bandgap lessening could be due to enhanced crystallinity.

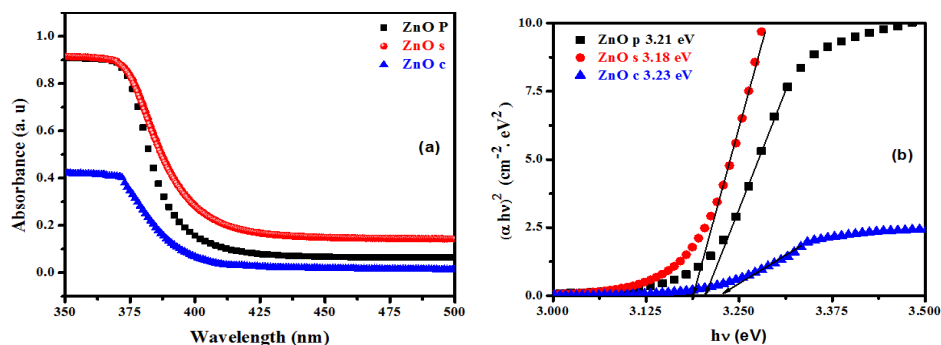


Fig. 4. (a) *Uv-vis spectra*, and (b) *bandgap in (eV) of ZnO nanoparticles prepared using different methods.*

### 3.4.2. Functional groups investigations

FTIR is a powerful technique adopted to identify the functional groups of ZnO nanoparticles fabricated employed different methods and the detection of the purity of nanomaterials constructed. FTIR spectra of all nanopowders designated in the range of 400–4000  $\text{cm}^{-1}$  are represented in Fig. 5. The vibration modes at 3435  $\text{cm}^{-1}$  are corresponding to the  $\text{H}_2\text{O}$  molecules [15]. The sharp peaks located at 1625  $\text{cm}^{-1}$  is associated with the bending vibration of H-O-H [5]. These peaks are founded from the little water molecule existing in ZnO p, ZnO s, and ZnO c nanoparticles surface as moisture [4]. Besides, for Zinc oxides (ZnO), hydroxyl group concentration represents the surface hole concentration [8], especially anion vacancies in nanomaterials [16]. Hence, the intensity of the hydroxyl groups' stretching vibration mode can approximate the surface defect concentration [17].

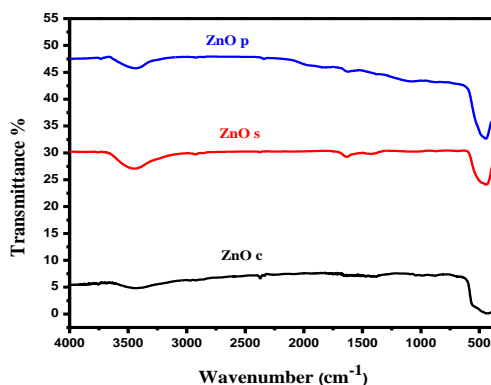


Fig. 5. *FTIR spectra of ZnO nanoparticles via various preparation methods.*

### 3.5. Thermogravimetric (TGA) analysis

Thermogravimetric (TGA) study of ZnO materials fabricated through precipitation, sol-gel, and combustion method were measured to examine the thermal stability. The as-prepared materials were burned from room temperature to 700°C with an increase of 10°C/min in air as shown Fig 6.

For ZnO c formation, the Zn@arabinose thermograph showed two-weight decline steps of the Zn@arabinose through the heating method. In the first step, within 160–300°C, weight decrease was produced by decomposing the arabinose sugar to tiny organic fragments like furan methanol,  $\alpha$ -angelica lactone, and methyl ester of furoic acid [18]. The weight destruction of the ZnO s nanoparticles creation occurs till 425°C, and the peaks are found at 120, 144, 200, and 390°C. These peaks are attributed to water and organics dehydration and decomposition of acetate. For ZnO p thermal stability, Fig 6 shows a slight mass decline at nearby 119 °C due to gaseous from the solvent and  $\text{H}_2\text{O}$  molecule desorption. The important mass loss stage seen in the range of

150 – 261°C temperature range could be describing the precursor breakdown step and the following CO<sub>2</sub> removal [19]. In the final stage after 425°C, no further mass loss was observed in all samples used to fabricate ZnO thin film solar cell devices.

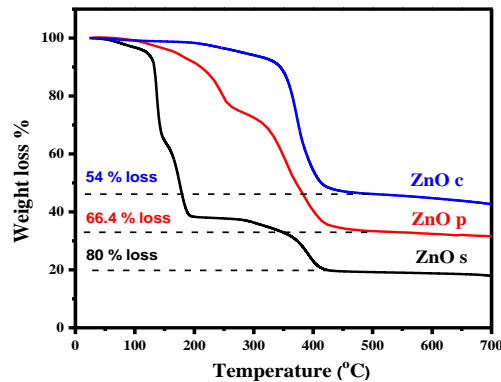


Fig. 6. Thermogravimetric analysis (TGA) for all ZnO samples before calcination at 700°C.

### 3.5. The electrical properties

Fabrication of ZnO thin films with high transmittance while maintaining electrical resistivity and sheet resistance as low as possible is the majority of studies' focal objective. The bulk electrical resistivity of a hexagonal wurtzite ZnO crystal structure is around  $10^2$  to  $10^4$

( $\Omega\cdot\text{cm}$ ) at 20 °C. ZnO thin films' electrical properties essentially dominate electrons produced from Zn interstitial atoms and oxygen vacancies. According to the semiconductors principle, the electrical conductivity of Zn directly proportional with the temperature.

Van der Pauw method applied to achieve Hall effect measurements. The applied magnetic field was 0.8 T. Aluminium dots were evaporated into square shapes as electrodes with dimensions (5 x 5 mm<sup>2</sup>). Variations electric characteristics ZnO thin films such as sheet resistance, resistivity, mobility, and carrier concentration with preparation methods are listed in table 3. All samples present have a similar crystal structure at thin films form, but a higher resistivity is recorded due to the thin film form and low-temperature annealing and ZnO films' low thickness. (28.2 n $\Omega\cdot\text{m}$  at 20 °C). films revealed a significant drop in carrier concentrations to be  $9.85 \times 10^{11}$  N (cm<sup>-3</sup>) for the maximum value. This can be attributed to the low density of ZnO thin films as observed in SEM images. A comparatively little variation in carrier mobility was received due to the tensile strain, partly counterbalancing the impact of the crystal structure's dislocations and the direct current stress on mobility degradation dominated in all samples.

Table 3. A summary of electrical properties of typical ZnO thin films deposited on Si substrates.

Samples	Sheet resistant ( $R_s$ ) ( $\Omega/\square$ )	Resistivity $\rho$ ( $\Omega\cdot\text{cm}$ )	Carrier concentration N (cm <sup>-3</sup> )	Hall mobility $\mu_H$ (cm <sup>2</sup> /V-s)
ZnO p	$73.5 \times 10^4$	11.2	$9.85 \times 10^{11}$	0.96
ZnO s	$96.0 \times 10^4$	8.5	$2.03 \times 10^{10}$	1.25
ZnO c	$49.9 \times 10^4$	5.5	$1.67 \times 10^{11}$	2.45

Solar cell simulator system with an incident light power of 1k watt/m<sup>2</sup> was used PV properties of fabricated devices. Figure 8 presents the(J-V) curves for illuminated ZnO/Si heterojunction, where (J) is the current density-and V is the open-circuit voltage. The values of PV output parameters are summarized in Table 4. The best sample (ZnO c) efficiency was limited 10%, with a Voc of 1.095 V, Jsc of 16.8 mA/cm<sup>2</sup>, and FF of 71%. This limitation can be attributed

to the low-temperature treatments. The increasing of the short circuit currents  $I_S$  without significant  $V_{OC}$  enhancements as shown in the insert figure can be returned to the diminished defects that are strongly associated with recombination loss, and can be considered the main reason for this loss. Moreover, the bigger grain size grew ZnO nanoparticles, progressing the density of the short circuit current. ZnO nanostructures nature cased the solar cell's efficiency by the light absorption enhancement due to their high specific surface area. Also, it can simultaneously enhance PV parameters by recrystallizing the films by more heat treatments at a higher temperature to minimized Ohmic contacts, and recombinative losses will have significantly increase the performance of the solar cell.

Table 4. ZnO/p-Si heterojunction solar cell performance characteristics.

Samples	J (Ma/cm <sup>2</sup> )	Voc (V)	FF (%)	Effcinicy( $\eta$ ) %
ZnO p	14.3	1.111	63	8.5
ZnO s	15.4	1.104	64	9
ZnO c	16.8	1.095	71	10

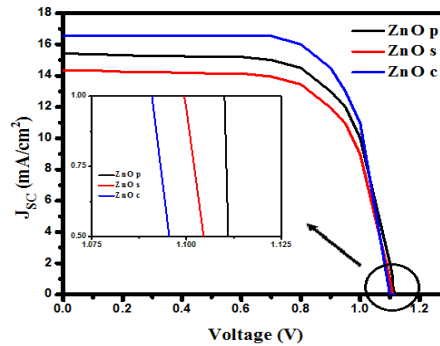


Fig. 8. J-V curves of ZnO/p-Si heterojunction solar cell.

#### 4. Conclusion

This work presented the synthesis of ZnO nanoparticle precursor solutions via three chemical reactions. The obtained solutions were spin-coated onto Si (111) substrate to achieve ZnO thin films with nanostructures that were employed to fabricate ZnO/Si heterojunction solar cells. The SEM analysis revealed the films' with not homogenous distribution on the substrate. The optioned set of ZnO films were showed polycrystalline nature having hexagonal wurtzite phase with crystallite sizes affected by the preparation technique. The optical band gaps ( $E_g$ ) of ZnO thin films were from the optical transmittances that were carried out via UV-vis dual-beam spectrophotometer. The computed  $E_g$  values show a significant change with variation of preparation technique. Based on the electrical properties of ZnO the samples were exhibited relatively high sheet resistance and resistivity. Besides the carrier concentrations, these resistors are strongly associated with the fabricated solar cell device's performance. The efficiencies can be considered promising due to the cost-effective preparation techniques

## Acknowledgments

The authors gratefully acknowledge the Deanship of Scientific Research at Imam Mohammad Ibn Saud Islamic University (IMSIU) Riyadh, Kingdom of Saudi Arabia, for financing this study through the research project No:381215

## References

- [1] S. R. Bathe, P. Patil, *Materials Science and Engineering: B* **257**, 114542 (2020).
- [2] D. Navas et al., *Heliyon* **6**(12), e05821 (2020).
- [3] R. Perveen et al., *Journal of Materials Research and Technology* **9**(4), 7817 (2020).
- [4] B. Y. Abdulkhair et al., *Zeitschrift für Naturforschung A* **74**(10), 937 (2019).
- [5] A. Modwi et al., *Journal of Materials Science: Materials in Electronics* **27**(12), 12974 (2016).
- [6] A. Modwi et al., *Journal of Materials Science: Materials in Electronics* **30**(15), 14714 (2019).
- [7] A. Modwi et al., *Journal of environmental chemical engineering* **5**(6), 5954 (2017).
- [8] C. Rajkumar, R. K. Srivastava, *Optical Materials* **109**, 110367 (2020).
- [9] M. Goswami, N. C. Adhikary, S. Bhattacharjee, *Optik* **158**, 1006 (2018).
- [10] C. Rajkumar, R. K. Srivastava, *Results in Physics* **15**, 102647 (2019).
- [11] A. Modwi et al., *Journal of Materials Science: Materials in Electronics* **29**(4), 2791 (2018).
- [12] V. Mote, Y. Purushotham, B. Dole, *Journal of Theoretical and Applied Physics* **6**(1), 6 (2012).
- [13] A. Modwi et al., *Journal of Materials Science: Materials in Electronics* **29**(3), 2184 (2018).
- [14] J. Li et al., *Ceramics International* **45**(3), 3871 (2019).
- [15] M. Gharagozlou, R. Bayati, *Materials Research Bulletin* **61**, 340 (2015).
- [16] N. Pauzi, N. M. Zain, N. A. A. Yusof, *Journal of Environmental Chemical Engineering* **8**(3), 103331 (2020).
- [17] S. W. Balogun et al., *Sn Applied Sciences* **2**(3), 1 (2020).
- [18] U. Räisänen et al., *Journal of thermal analysis and calorimetry* **72**(2), 481 (2003).
- [19] Z. Siqingaowa, H. Yao, *Frontiers of Chemistry in China* **1**(3), 277 (2006).